Supplementary Information

High-Throughput Functional Profiling of Single Adherent Cells via Hydrogel Drop-Screen

Ming Wang[a,b,c], Mui Hoon Nai[b], Yun-Ju Ruby Huang[d,e,f], Hwa Liang Leo[a,b], Chwee Teck Lim[a,b,c,g] and Chia-Hung Chen[h]*

a. Department of Biomedical Engineering, National University of Singapore, 4 Engineering Drive 3, Singapore 117583
b. NUS Graduate School for Integrative Sciences and Engineering, National University of Singapore, 21 Lower Kent Ridge Road 04-02, Singapore 119077
c. Institute for Health Innovation and Technology (iHealthtech), MD6, 14 Medical Drive 14-01, Singapore 117599
d. Mechanobiology Institute, National University of Singapore, Singapore 117411
e. School of Medicine, College of Medicine, National Taiwan University, No.1 Jen-Ai Road, Taipei, Taiwan, 10051
f. Graduate Institute of Oncology, College of Medicine, National Taiwan University, No. 1, Sec. 4, Roosevelt road, Taipei, Taiwan, 10617
g. Department of Biomedical Engineering, National Taiwan University, No.1, Sec.1, Jen-Ai Road, Taipei, Taiwan, 10051
h. Department of Biomedical Engineering, City University of Hong Kong, Y6700, 83 Tat Chee Avenue, Hong Kong SAR, China, E-mail: chiachen@cityu.edu.hk

Content:

Supplementary-1: Physiological extracellular matrix (ECM) stiffness

The human body consists of diverse cell types that accomplish a vast range of functions. Each individual cell type has its own optimal environment. The range of physiologically relevant stiffnesses of both healthy and cancerous ECMs is shown (**Figure S1**). In general, healthy tissues are soft and have an elasticity ≤ 10 kPa, while the ECM of cancer cells is stiff with an elasticity of ≥10 kPa. For instance, when hepatocytes are subjected to a stiffer ECM, cell cycle progression and dedifferentiation are elevated[1]. It is desirable to provide an ECM with stiffness matching the natural cell requirement for analysis. ECM stiffness in the human body ranges from a few pascals to gigapascals. In this study, the cancer cells on gelatin particles with a stiffness of 10-100 kPa were measured.

In the case of brain tumors, the range of ECM stiffness is from 0.17 kPa (healthy) to 35 kPa, depending on pathologies[2, 3]. In the case of breast tumors, the range is from 0.85 kPa (non-cancerous) to 120 kPa[4-6]. The ECM stiffness of lung cancer varies from 0.2 kPa (healthy) to 100 kPa (both fibrotic and nonfibrotic)[7-9]. The ECM of bladder tumors could vary considerably in a short period of time depending on the volume of urine present: 10 to 500 kPa[10-12]; lymphoma typically has an ECM stiffness of 10 to 100 kPa[13-15]; the stiffness of colorectal cancer ECM ranges from 1 to 70 kPa[16, 17]; and both bone cancer and leukemia grow in osteoids with a stiffness from 0.2 to 100 kPa[18-20]. In the case of the liver, the stiffness ranged from 2 kPa (healthy) to 75 kPa[21-24]. The stiffness of prostate ECM ranges from 1 kPa (healthy) to 90 kPa[25-27]. The stiffness of ECMs of various cancers is summarized in **Table S1**.
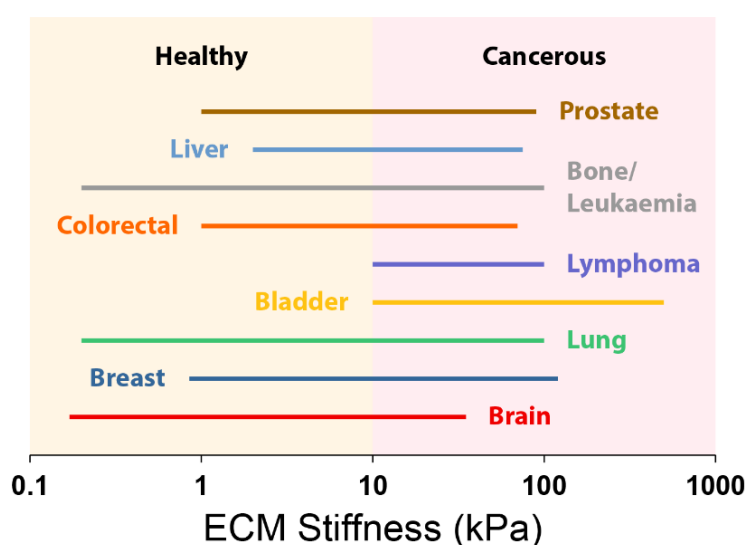

Figure S1. The physiologically relevant ECM stiffness of healthy and cancerous patients ranges from 0.1 kPa to 1000 kPa.

Table S1. Physiologically relevant ECM stiffness of various cancers.

Cancer Type	Lowest stiffness (healthy/benign)	Highest stiffness (malignant)	Reference
Brain	0.17 kPa	35 kPa	[2, 3]
Breast	0.85 kPa	120 kPa	[4-6]
Lung	0.2 kPa	100 kPa	[7-9]
Bladder	10 kPa (unloaded)	500 kPa (loaded)	[10-12]
Lymphoma	10 kPa	100 kPa	[13-15]
Colorectal	1 kPa	70 kPa	[16, 17]
Bone/Leukemia	0.2 kPa	100 kPa	[18-20]
Liver	2 kPa	75 kPa	[22-24]
Prostate	1 kPa	90 kPa	[25-27]

Supplementary-2: Staining dyes
Table S2: Peak excitation and emission wavelengths of the staining dyes used.

Stain	Fluorophore	Peak excitation wavelength	Peak emission wavelength
Nucleus	Hoechst 33342	352 nm	455 nm
Cytosol	Fluorescein	498 nm	517 nm
Plasma membrane	DiI	551 nm	569 nm
F-actin	Alexa Fluor 647	650 nm	671 nm

Supplementary-3: Device design for cell morphological analysis

The single cell morphology was screened by using a microfluidic device with a flow focusing channel, whose nozzle size was 30×30 μm in diameter (**Figure S2**).
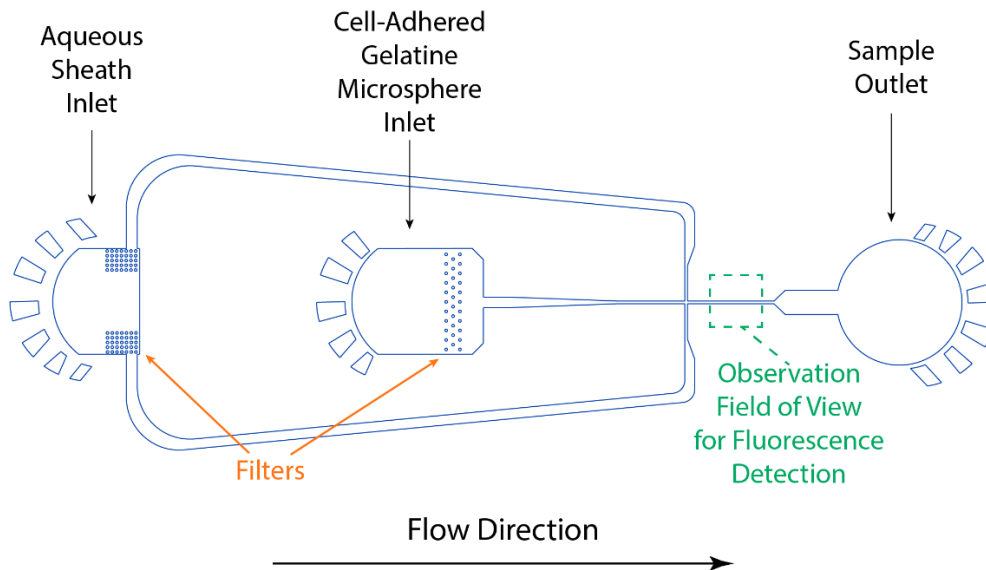

Figure S2. Microfluidic design to screen single cells adhered on gelatin particles.

Supplementary-4: Device design for gelatin particle encapsulation

The device design to produce droplets encapsulating cell-adhered gelatin particles and FRET sensors is included (**Figure S3**). A flow focusing device with a nozzle (dimension of 45×60 μm^2) was fabricated to align the gelatin particles (diameter of 30 μm) to allow one passage per time in order. The T-junction at which the FRET sensors were introduced (dimensions of 20×60 μm^2) for assays is also shown.
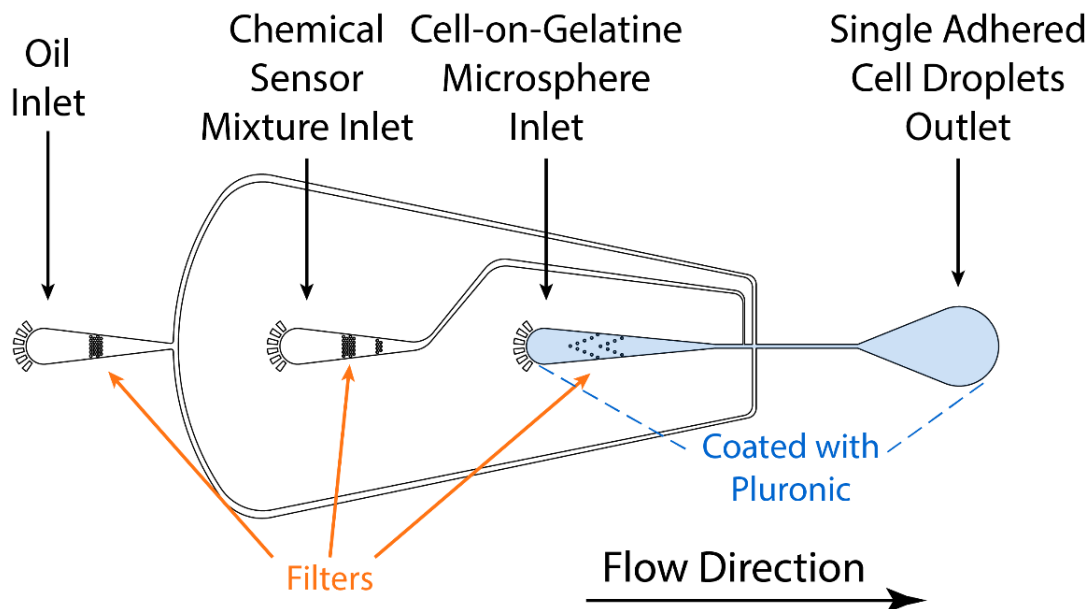
Figure S3. A microfluidic device for the single gelatin particle and chemical sensor mixture (FRET substrates) encapsulation in water-in-oil droplets was fabricated.

Supplementary-5: Drop-hydrogel screen device design

The fluorescence signals from each droplet were measured in a device with a flow focusing channel. This nozzle size was 80×80 μm^2 in dimensions (**Figure S4**).

Figure S4. Microfluidic design for droplet-based hydrogel screening to measure single cell secretions of ADAMs/MMPs within the droplets at a throughput of ~100 cells/second.

Supplementary-6: Optical system
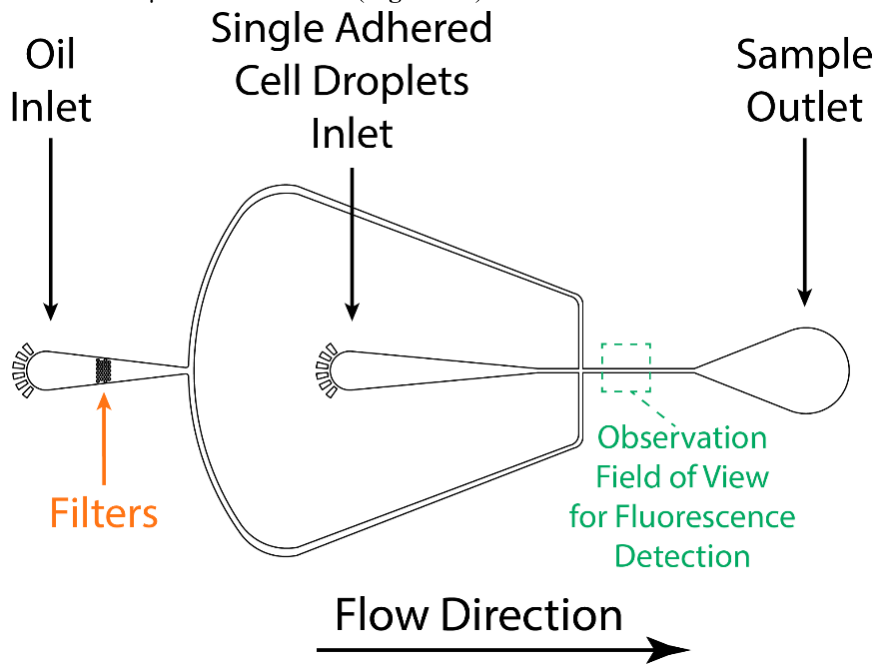
The optical system was constructed by an LED light (SOLA-SE-II, Lumencor, USA), whose excitation light was filtered by a multibandpass filter (89402x, Chroma, Taiwan) and deflected to sample with a multibandpass beam-splitter (89402bs, Chroma, Taiwan). The emission light passed through the same multibandpass beamsplitter, deflected by the respective dichroic mirrors T495LPxr (Chroma, Taiwan), T565LPxr (Chroma, Taiwan), and T660Lpxr (Chroma, Taiwan), followed by passing through the emission filters ET460/50m (Chroma, Taiwan), ET525/50m (Chroma, Taiwan), ET605/70m (Chroma, Taiwan), and ET690/50m (Chroma, Taiwan) (**Table S3**) prior to detection. The fluorescence signals were then recorded by PMTs. The four sets of excitation/emission channels used are noted as UV, Blue, Green, and Red, respectively.

Table S3: Specifications of excitation/emission filters and dichroic mirrors

Filter/ dichroic mirror	Optical Channel							
	Excitation Wavelength (nm)				Emission Wavelength (nm)			
	UV	Blue	Green	Red	UV	Blue	Green	Red
89402x (Excitation filter)	375-407 (T>95%)	462-495 (T>95%)	541-566 (T>95%)	621-653 (T>95%)				
89402bs (Beamsplitter)	<410 (R>95%)	459-497 (R>97%)	538-569 (R>94%)	619-655 (R>97%)	413-456 (T>95%)	504-535 (T>95%)	573-614 (T>97%)	660-735 (T>97%)
T495LPxr (Dichroic mirror 1)					<493 (R>90%)	>499 (T>95%)		
ET460/50m (Emission filter 1)					436-484 (T>95%)			
T565LPxr (Dichroic mirror 2)						<560 (R>95%)	>568 (T>97%)	
ET525/50m (Emission filter 2)						501-547 (T>97%)		
T660Lpxr (Dichroic mirror 3)							<660 (R>95%)	>667 (T>95%)
ET605/70m (Emission filter 3)							572-638 (T>97%)	
ET690/50m (Emission filter 4)								668-718 (T>95%)
Summary								
Effective window	Excitation				Emission			
	375-407	462-495	541-566	621-653	436-456	504-535	573-614	668-718

Stains for morphological study								
Stain/Substrate	Nucleus	Cytosol	Plasma Membrane	F-actin	Nucleus	Cytosol	Plasma Membrane	F-actin
Fluorophore Peak	352	498	551	650	455	517	569	671
Substrates for secretory study								
	Collective activities of metalloproteinase families							
Stain/Substrate	Nucleus	ADAM		MMP	Nucleus	ADAM		MMP
Fluorophore Peak	352	490		635	455	520		670
	Proteolytic Activity Matrix Analysis (PrAMA)							
Stain/Substrate	Nucleus	Blue	Green	Red	Nucleus	Blue	Green	Red
Fluorophore Peak	352	490	546	635	455	520	589	670

T: Transmission efficiency; R: Reflection efficiency at 45°

Supplementary-7: Optimization of the cell seeding ratio

The cells were incubated with gelatin particles in a 6-well ultralow attachment culture plate (Corning, USA) and a 2 ml microcentrifuge tube (AITbiotech, Singapore) for cell adhesion. For single cell attachment to gelatin particles, the seeding ratios between cells (A549 cells) and particles are optimized. The result indicated that the optimized seeding ratio was 3:1 (cells to gelatin particles) (**Figure S5**).
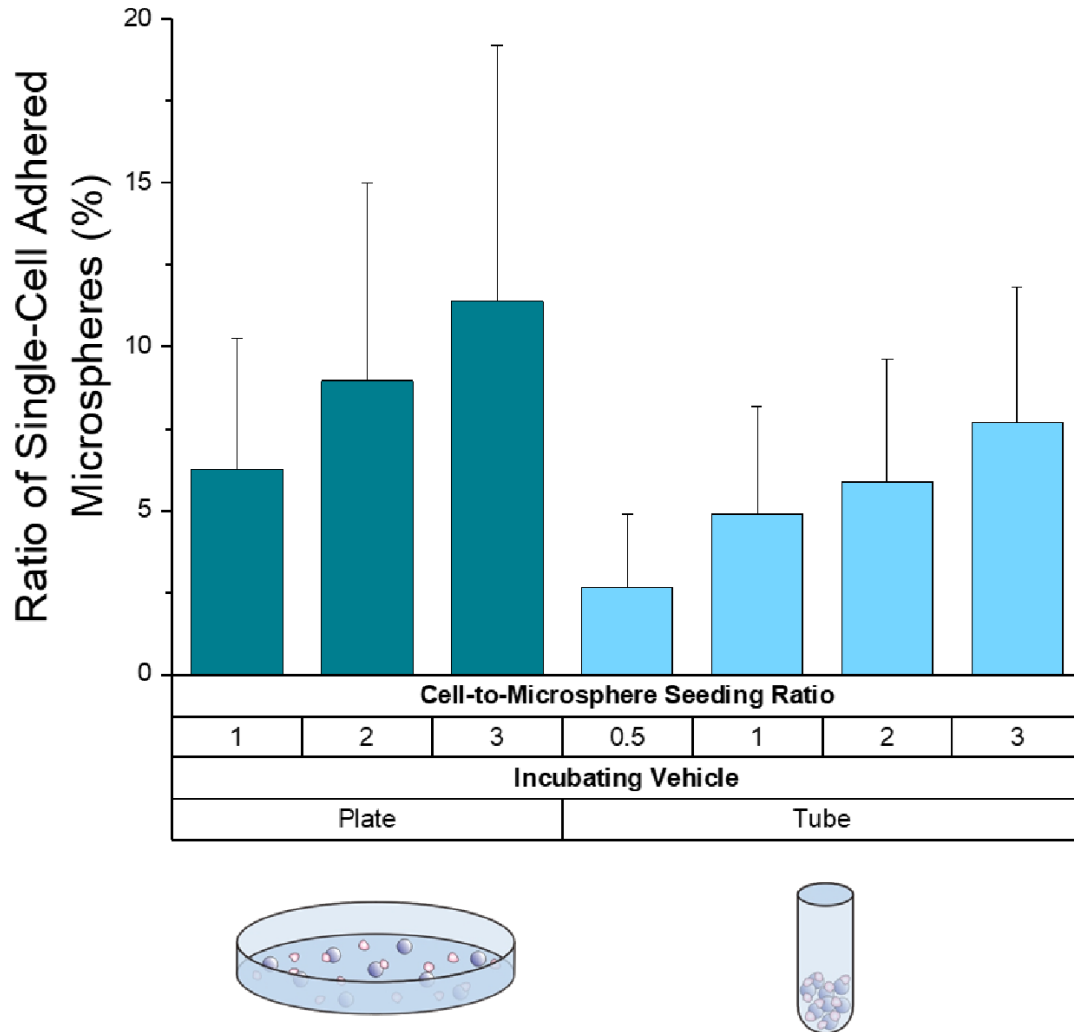

Figure S5. Optimization of cell seeding ratios of cell to gelatin particles.

Supplementary-8: Gelatin particle size optimization

The size of gelatin particles was optimized for single-cell attachment. In the case of large gelatin particles (120 μm in diameter), ~40% of the particles had cell(s) attached. However, only 2% of particles had single cell attached; 38% of the particles were attached with multiple cells. In the case of small gelatin particles (30 μm in diameter), ~16% of the particles had cell(s) attached. Approximately 14% of the gelatin particles were attached with single cell, while 2% of the particles were attached with multiple cells (**Figure S6**). Although the cells effectively adhere to large gelatin particles, the single-cell attachment rate was low. In the case of large gelatin particles, most particles were adhered with multiple cells, limiting the efficiency of the single-cell assay. Based on the observation, small gelatin particles (30 m in diameter) were used in the experiments of our droplet-based hydrogel screening.
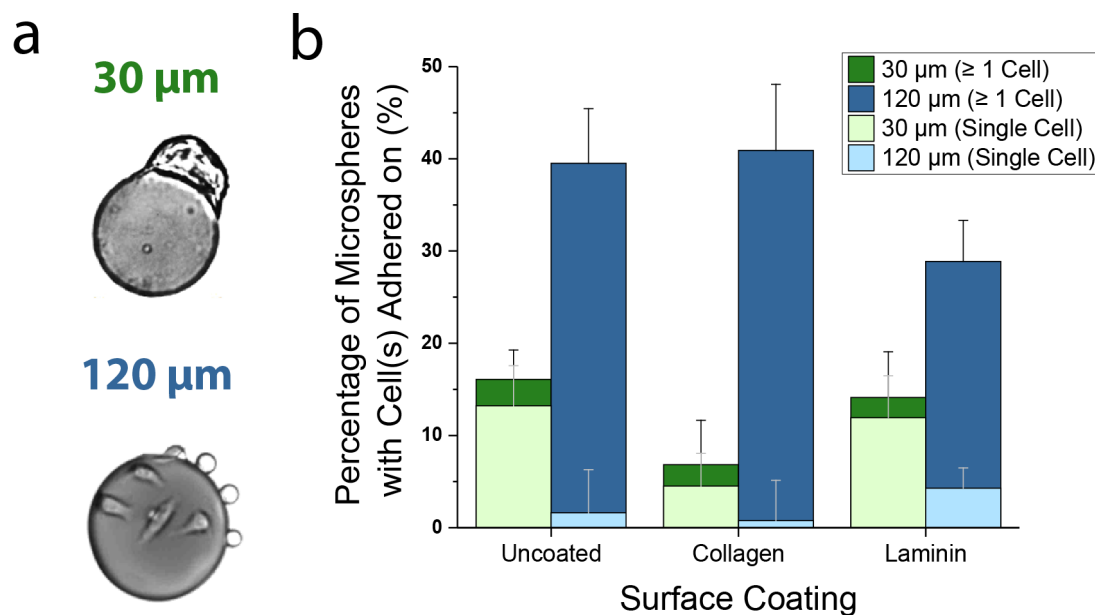

Figure S6. Optimization of gelatin particles. (a) A549 cells adhered to gelatin microspheres with diameters of 30 μm and 120 μm. (b) Effects of sizes and surface coatings on cell adhesion onto gelatin particles. The seeding ratios of cells and gelatin particles during incubation for cell adhesion were identical for all experiments (3:1).

Supplementary-9: Data processing (noise filtering)

(a) Filtering: Data collected from PMTs were filtered by using a low-pass filter (LFP) with finite impulse response (FIR) to remove white noise and systematic noises, such as noise from the electric circuit of neighboring machines. The cut-off frequency was set at 300 Hz, and the filter order was set at 150. The protocol is indicated in the following section.

(b) Optimization of cut-off frequency: The cut-off frequency is important to determine the efficiency of a frequency-based filter system. The low cut-off frequency is set to filter out the noise. However, the signal might be overfiltered if the cut-off frequency is too low. After optimization, in this study, the cut-off frequency was set to 300 Hz (**Figure S7**).

(c) Normalization by using droplets containing trypsin and FRET sensors as a positive control: Many systematic errors might affect the accuracy of the experimental data collected. For consistency of the experimental results, in each experiment, the freshly prepared FRET sensor mixture of each experiment was reacted with trypsin for 30 min at 37 °C and encapsulated into droplets to record the fluorescence increases as the positive controls.
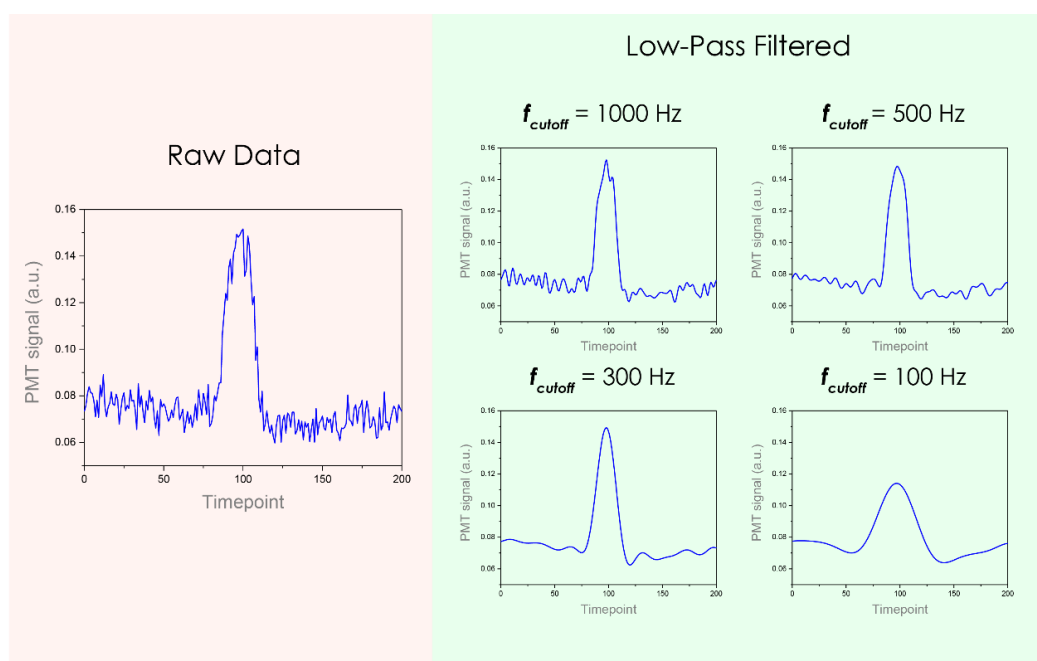

Figure S7. Signal waveforms of fluorescence signals detected by PMT as raw data and after low-pass filtering with 1000 Hz, 500 Hz, 300 Hz, and 100 Hz as cut-off frequencies.

Supplementary-10: Single cell PMT fluorescence signal calibration

To differentiate signals from droplet containing single cell or multiple cells collected by PMT, the Hoechst intensities in different situations were characterized. The cells were stained by using Hoechst 33342 (1 µg/ml, Sigma-Aldrich, USA) for 24 hours. There were two peaks observed by using PMT (**Figure S8a**). The first peak represents the droplets with a single-cell adhered gelatin particle, while the second peak represents the gelatin particles with two cells attached. The discrete frequency distribution of Hoechst intensities was first converted to a continuous plot (**Figure S8b**), followed by smoothing with a low pass-filter (**Figure S8c**). The prominence of the peak corresponding to single cell was identified. Based on that, the width at half-prominence was estimated. The range of Hoechst intensity corresponding to single cells was determined as

$$\text{Hoechst Intensity at Prominence} \pm \text{Width at Half-Prominence}$$

In our experiment, the rage of Hoechst intensity corresponding to single cells was $0.1345 \pm 0.0368 = 0.0977 \sim 0.1713$ (**Figure S8d**). All the data outside this range were considered as non-single cell situations and were omitted to ensure that the data collected were single cell data.
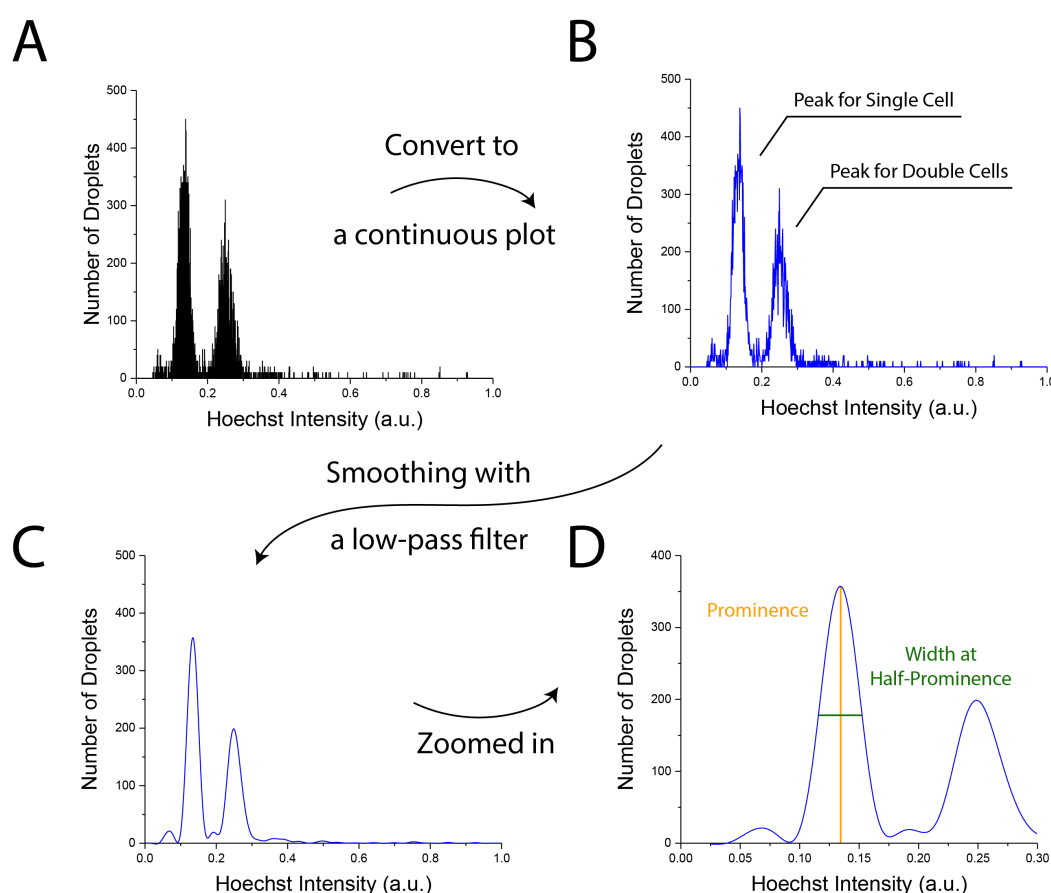
Figure S8. Single cell data recorded by PMT: (a) When recording Hoechst fluorescence signals in the droplets, two peaks were observed: one referred to single cell encapsulation situation, the other referred to multiple (two) cells encapsulation situation, respectively. (b) The discrete frequency distribution plot was converted to a continuous plot. (c) The plot was smoothened by using a low-pass filter. (d) The range of peak, indicating signal corresponding to single-cell adhered gelatin particle in the droplets was identified (the left hand side main peak).

Supplementary-11: Proteolytic activity matrix analysis (PrAMA)

Proteolytic activity matrix analysis (PrAMA) is a computational method for determining the specific enzymatic activities of a disintegrin and metalloproteinases (ADAMs) and matrix metalloproteinases (MMPs). PrAMA uses a mathematical model to simultaneously calculate various MMP and ADAM activities from an activity-based assay with a couple of FRET sensors. The governing equation to process PrAMA is indicated below. The catalytic efficiency was determined by performing experiment with pure ADAMs/MMPs (**Figure S9**).

$$V_{0,i} = [S_i] \sum C_{i,j} [E_j]$$

where $V_{0,i}$ denotes the initial rate of FRET sensor cleavage by metalloproteinases

        S_i denotes the respective FRET sensor concentrations

        $C_{i,j}$ denotes the catalytic efficiency of individual metalloproteinases to respective FRET sensors (i^{th} FRET sensor and j^{th} metalloproteinase, refer to the Catalytic Efficiency Matrix below)

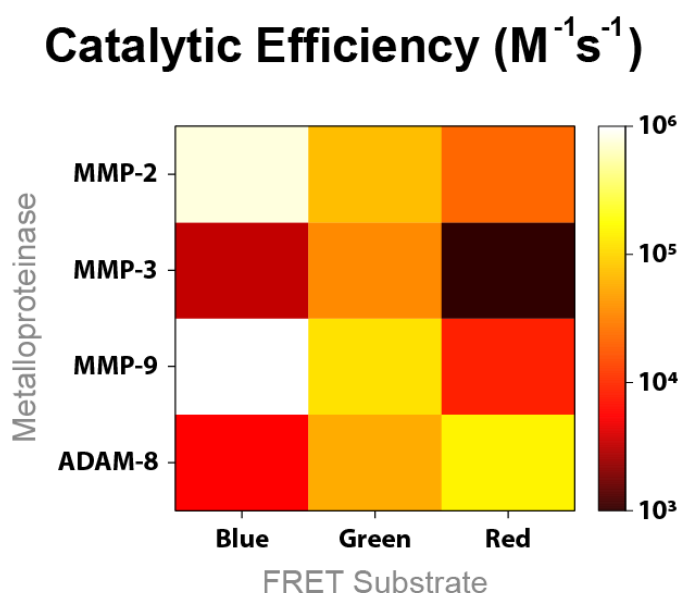 E_j denotes the active concentrations of respective metalloproteinases

Figure S9. Catalytic efficiency matrix for PrAMA. Individual catalytic efficiencies were characterized with respective customized FRET sensors (Supplementary 7) and pure metalloproteinases.

Supplementary-12: Fluorescence resonance energy transfer (FRET) sensors

Fluorescence resonance energy transfer (FRET) sensors were used to quantify the enzymatic activities of ADAMs and MMPs secreted by or docked to the plasma membrane of the cells (**Table S4**). Three FRET sensors with different fluorophores and quenchers were designed to evaluate the activities of the individual ADAM and MMP (**Table S5**). In this study, MMP2, MMP3, MMP9, and ADAM8 activity was determined via PrAMA, revealing the potential of cell migration and metastasis.

Table S4: Customized FRET sensors for detecting collective ADAM and MMP activities

Name	Sequence	Peak Excitation Wavelength	Peak Emission Wavelength
MMP	QSY21-Pro-Cha-Cys(Me)-His-Ala-Lys(Cy5)-NH2	635 nm	670 nm
ADAM	Dabcyl-Pro-Arg-Ala-Ala-Ala-HPhe-Thr-Ser-Pro-Lys(5FAM)-NH2	490 nm	520 nm

Table S5: Customized FRET sensors for detecting individual ADAM and MMP activities

Name	Sequence	Peak Excitation Wavelength	Peak Emission Wavelength
Blue	Dabcyl-Gly-Pro-Leu-Gly-Met-Arg-Gly-Lys(5-FAM)-NH2	490 nm	520 nm
Green	QSY7-Ala-Pro-Phe-Glu-Met-SerAla-Lys(5TAMRA)-DArg-NH2	546 nm	589 nm
Red	QSY21-His-Gly-Asp-Gln-Met-Ala-Gln-Lys-Ser-Lys(Cy5)-NH2	635 nm	670 nm

Supplementary-13: Heat map to evaluate single cell enzyme activities

To illustrate single cell MMPs and ADAM activities, a heat map was constructed by using PrAMA (**Figure S10**). It was found that, only a small population of cells expressed high MMP9 activity. These cells mostly expressed lower activities in MMP2 and MMP3. MMP3 is the most expressed metalloproteinase by the cells (except for MCF10A cells). For MCF7 and MDA-MB-231 cancer cells, the majority (80~90%) of the cell population expressed high MMP3 activities. There was a certain percentage of cells (10%), exhibiting high activities in all metalloproteinases in MDA-MB-231 cells on stiff substrate (100 kPa). However, there were ~2% MDA-MB-231 cells on soft substrate (70 kPa) expressed high activities in all metalloproteinases. For MCF7 cells oh stiff/soft substrate, there was ~1-2% of the cells expressed high activities in all metalloproteinases.
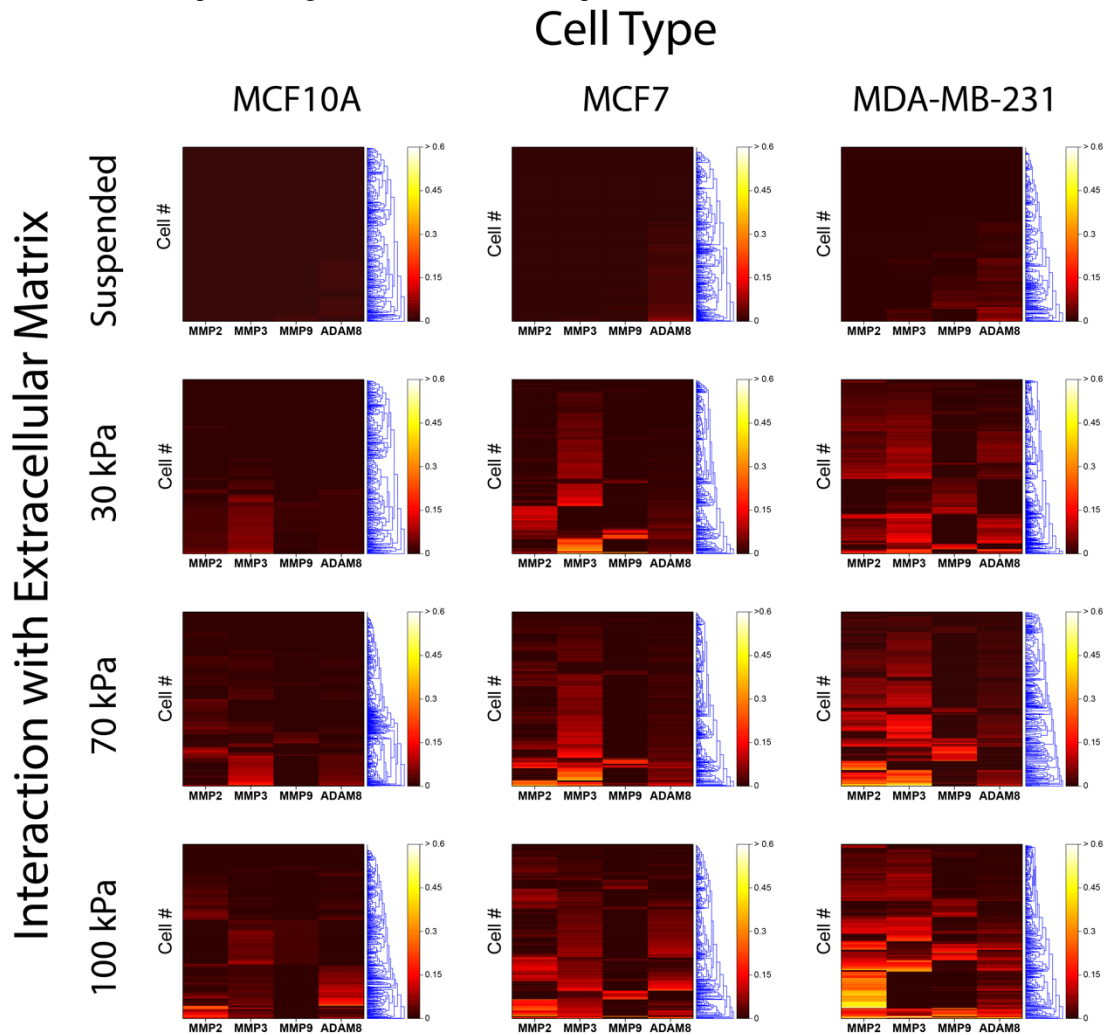

Figure S10. Heat map to evaluate single cell MMPs and ADAMs activities of MCF10A, MCF7, and MDA-MB-231 cells. Euclidean distance was adopted for clustering and the hierarchical clustering maps are indicated in blue.

Supplementary-14: Quantification of heterogeneity

In order to compare the heterogeneities of respective cell types when they were adhered to different matrix stiffnesses, the heterogeneity (dispersion of data) was quantified with the standard deviations of the four metalloproteinase activities. Prior to the computation of standard deviations, all the data were normalised with the largest value of the local dataset to avoid bias due to the magnitude of the metalloproteinase activity.

$$Heterogeneity, \tau = \sqrt{\sigma_{MMP2}^2 + \sigma_{MMP3}^2 + \sigma_{MMP9}^2 + \sigma_{ADAM8}^2}$$

Table S6: Standard deviations of respective metalloproteinase activities and heterogeneity of different cell types adhered to different matrix stiffnesses

| Cell	Stiffness	σ_{MMP2}	σ_{MMP3}	σ_{MMP9}	σ_{ADAM8}	Heterogeneity (τ)
MCF-10A	Suspended	0.0003	0.0010	0.0028	0.0042	0.0052
	30 kPa	0.0117	0.0320	0.0049	0.0065	0.0350
	70 kPa	0.0222	0.0380	0.0104	0.0157	0.0478
	100 kPa	0.0477	0.0221	0.0089	0.0456	0.0702
MCF-7	Suspended	0.0006	0.0040	0.0030	0.0191	0.0197
	30 kPa	0.0366	0.0742	0.0473	0.0165	0.0967
	70 kPa	0.0611	0.0722	0.0361	0.0264	0.1046
	100 kPa	0.0652	0.0397	0.0403	0.0476	0.0986
MDA-MB-231	Suspended	0.0012	0.0062	0.0110	0.0193	0.0231
	30 kPa	0.0336	0.0479	0.0330	0.0444	0.0805
	70 kPa	0.0792	0.0841	0.0483	0.0250	0.1276
	100 kPa	0.1268	0.0795	0.0717	0.0517	0.1738
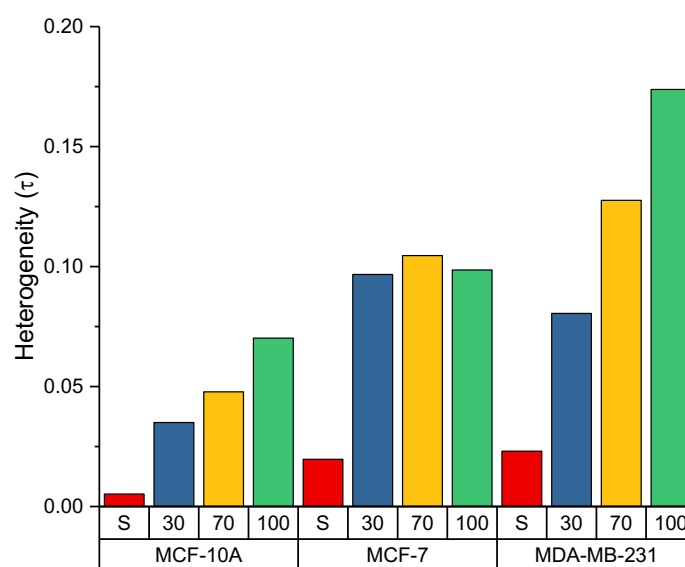
Figure S11. Heterogeneity of the metalloproteinase activities expressed by different cells when they were adhered to different matrix stiffnesses. (S: suspended, 30/70/100: magnitude of matrix elastic modulus in kPa)

References

1.   Hansen LK, Wilhelm J, Fassett JT. Regulation of Hepatocyte Cell Cycle Progression and Differentiation by Type I Collagen Structure. In: *Current Topics in Developmental Biology* (ed^(eds). Academic Press (2005).

2.   Stewart DC, Rubiano A, Dyson K, Simmons CS. Mechanical characterization of human brain tumors from patients and comparison to potential surgical phantoms. *PloS one* **12**, e0177561-e0177561 (2017).

3.   Chauvet D*, et al.* In Vivo Measurement of Brain Tumor Elasticity Using Intraoperative Shear Wave Elastography. *Ultraschall Med* **37**, 584-590 (2016).

4.   Hawley JR, Kalra P, Mo X, Raterman B, Yee LD, Kolipaka A. Quantification of breast stiffness using MR elastography at 3 Tesla with a soft sternal driver: A reproducibility study. *J Magn Reson Imaging* **45**, 1379-1384 (2017).

5.   Denis M*, et al.* Correlating Tumor Stiffness with Immunohistochemical Subtypes of Breast Cancers: Prognostic Value of Comb-Push Ultrasound Shear Elastography for Differentiating Luminal Subtypes. *PloS one* **11**, e0165003-e0165003 (2016).

6.   Evans A*, et al. Does shear wave ultrasound independently predict axillary lymph node metastasis in women with invasive breast cancer?* (2013).

7.   Burgstaller G, Oehrle B, Gerckens M, White ES, Schiller HB, Eickelberg O. The instructive extracellular matrix of the lung: basic composition and alterations in chronic lung disease. *European Respiratory Journal* **50**, 1601805 (2017).

8.   Miyazawa A*, et al.* Regulation of PD-L1 expression by matrix stiffness in lung cancer cells. *Biochem Biophys Res Commun* **495**, 2344-2349 (2018).

9.   Chen Y-L, Shih J-Y, Wang H-C, Wu H-D. The Predictive Value of Transthoracic Shear-Wave Ultrasound Elastography in Differentiating Benign from Malignant Lung Tumors. In: *A110. NOVEL IMAGING FOR LUNG CANCER: A PICTURE IS WORTH A THOUSAND WORDS* (ed^(eds).

10.   Nenadic IZ*, et al.* Ultrasound bladder vibrometry method for measuring viscoelasticity of the bladder wall. *Phys Med Biol* **58**, 2675-2695 (2013).

11.   Lekka M, Pabijan J, Orzechowska B. Morphological and mechanical stability of bladder cancer cells in response to substrate rigidity. *Biochim Biophys Acta Gen Subj* **1863**, 1006-1014 (2019).

12.   Li C*, et al.* Quantitative elasticity measurement of urinary bladder wall using laser-induced surface acoustic waves. *Biomed Opt Express* **5**, 4313-4328 (2014).

13.   Kim Y, Ko KH, Jung HK, Lee HJ. Shear-Wave Elastography Features of Primary Non-Hodgkin's Lymphoma of the Breast: A Case Report and Literature Review. *J Clin Diagn Res* **10**, TD01-TD03 (2016).

14.   Choi YJ, Lee JH, Baek JH. Ultrasound elastography for evaluation of cervical lymph nodes. *Ultrasonography* **34**, 157-164 (2015).

15.   Bae SJ*, et al.* Ex Vivo Shear-Wave Elastography of Axillary Lymph Nodes to Predict Nodal Metastasis in Patients with Primary Breast Cancer. *J Breast Cancer* **21**, 190-196 (2018).

16.   Kawano S*, et al.* Assessment of elasticity of colorectal cancer tissue, clinical utility, pathological and phenotypical relevance. *Cancer Sci* **106**, 1232-1239 (2015).

17.   Brauchle E*, et al.* Biomechanical and biomolecular characterization of extracellular matrix structures in human colon carcinomas. *Matrix Biol* **68-69**, 180-193 (2018).

18.   Jansen LE, Birch NP, Schiffman JD, Crosby AJ, Peyton SR. Mechanics of intact bone marrow. *Journal of the Mechanical Behavior of Biomedical Materials* **50**, 299-307 (2015).

19. Buxboim A, Ivanovska IL, Discher DE. Matrix elasticity, cytoskeletal forces and physics of the nucleus: how deeply do cells 'feel' outside and in? *J Cell Sci* **123**, 297-308 (2010).

20. Tse JR, Engler AJ. Preparation of hydrogel substrates with tunable mechanical properties. *Curr Protoc Cell Biol* **Chapter 10**, Unit 10.16 (2010).

21. Fung J*, et al.* Defining normal liver stiffness range in a normal healthy Chinese population without liver disease. *PloS one* **8**, e85067-e85067 (2013).

22. Merchante N*, et al.* Liver stiffness predicts clinical outcome in human immunodeficiency virus/hepatitis C virus-coinfected patients with compensated liver cirrhosis. *Hepatology* **56**, 228-238 (2012).

23. Lee DH*, et al.* Liver Stiffness Measured by Two-Dimensional Shear-Wave Elastography: Prognostic Value after Radiofrequency Ablation for Hepatocellular Carcinoma. *Liver Cancer* **7**, 65-75 (2018).

24. Masuzaki R*, et al.* Assessing liver tumor stiffness by transient elastography. *Hepatol Int* **1**, 394-397 (2007).

25. Correas JM, Tissier AM, Khairoune A, Khoury G, Eiss D, Hélénon O. Ultrasound elastography of the prostate: State of the art. *Diagnostic and Interventional Imaging* **94**, 551-560 (2013).

26. Woo S, Kim SY, Cho JY, Kim SH. Shear wave elastography for detection of prostate cancer: a preliminary study. *Korean J Radiol* **15**, 346-355 (2014).

27. Glybochko PV*, et al.* [Prostate cancer detection by assessing stiffness of different tissues using shear wave ultrasound elastog- raphy]. *Urologiia*, 56-61 (2016).